

Phase decomposition of $\text{La}_2\text{NiO}_{4+\delta}$ under Cr- and Si-poisoning conditions

N. Schrödl¹, A. Egger¹, C. Gspan², T. Höschen³, F. Hofer², W. Sitte¹

¹Chair of Physical Chemistry, Montanuniversität Leoben, Franz-Josef-Straße 18, 8700 Leoben, Austria

²Institute for Electron Microscopy and Nanoanalysis (FELMI), Graz University of Technology & Graz

Centre for Electron Microscopy (ZFE), Steyrergasse 17, 8010 Graz, Austria

³Max Planck Institute for Plasma Physics, Boltzmannstraße 2, 85748 Garching, Germany

Abstract

The influence of simultaneous Cr- and Si-poisoning on the oxygen exchange kinetics of $\text{La}_2\text{NiO}_{4+\delta}$ was studied at 800°C in dry and humid O_2/Ar atmospheres over a period of 4000 hours by means of dc-conductivity relaxation measurements. Chemical and morphological changes of the $\text{La}_2\text{NiO}_{4+\delta}$ surface exposed to increasingly harsh ambient conditions were investigated using X-ray photoelectron spectroscopy (XPS) depth profiling, scanning electron microscopy with energy dispersive X-ray spectroscopy (SEM-EDXS) and high-resolution scanning transmission electron microscopy with energy dispersive X-ray and electron energy loss spectroscopy (HR-STEM EDXS/EELS). In the presence of Cr/Si-sources and under dry conditions, $\text{La}_2\text{NiO}_{4+\delta}$ shows good stability for more than 1000 hours. However, as soon as humidity is introduced into the system a strong decline of the oxygen exchange activity is observed. Post-test analyses reveal newly formed partially blocking Cr- and Si-rich secondary phases on the surface of $\text{La}_2\text{NiO}_{4+\delta}$ which impede the surface exchange of oxygen.

Keywords: SOFC cathode, Cr-poisoning, Si-poisoning, degradation

*Corresponding author: Dr. Andreas Egger, Chair of Physical Chemistry, Montanuniversitaet Leoben, Franz-Josef-Straße 18, 8700 Leoben, Austria; tel.: +43 3842 402 4814; fax: +43 3842 402 4802; e-mail address: andreas.egger@unileoben.ac.at

1 Introduction

Solid oxide fuel cells (SOFCs) are highly efficient energy conversion devices for stationary and mobile applications, which are usually operated in a temperature range of 800-1000°C. However, limitations to long-term stability at these high temperatures as well as high production costs pose a serious hindrance to large-scale commercialization of this promising technology. The need to develop advanced fuel cells with improved durability and lower production costs has led to a reduction of operating temperatures to 600-800°C, which allows for the use of cheaper materials in SOFC stacks. Metallic interconnects made of ferritic stainless steels exhibit high electronic and thermal conductivity as well as good machinability at intermediate temperatures and thus can replace ceramic interconnects [1]. Interconnect alloys usually contain large amounts of Cr in order to resist high temperature corrosion through Cr₂O₃ scale formation under typical SOFC operating conditions [2]. Chromia-rich scales can produce volatile, hexavalent Cr-species like chromium oxide (CrO₃) and – in the presence of air moisture – chromium oxyhydroxide (CrO₂(OH)₂) [3], which can be deposited on the cathode surface and lead to a long-term decrease in cell performance [4-6]. The application of protective barrier coatings based on rare earth perovskite or spinel structures has successfully reduced the emanation of Cr-species from interconnects [7,8], but poor layer adhesion, residual porosity or crack

formation in these coatings can lead to Cr-migration and Cr-poisoning of the SOFC cathode [9,10].

Similar performance deterioration has been observed in conjunction with the deposition of volatile Si-species [11-13]. Present as an impurity in raw materials – often introduced by powder and ceramics processing – as well as in silicate-based SOFC glass sealings, Si tends to form H_4SiO_4 as the dominant gas species in humid, oxidizing atmospheres [14,15]. Both Si and Cr effectively inhibit the incorporation of oxygen into the cathode material by blocking active sites for the oxygen exchange reaction and by forming electrically insulating reaction products with the cathode material.

In the literature, Cr-poisoning has frequently been associated with the segregation of a nucleation agent to the active surface, facilitating the deposition of Cr-species [16]. In strontium-containing state-of-the-art cathode materials like LSC and LSCF, SrO has been identified as nucleation agent for volatile Cr-species [4,17,18]. Moreover, Sr has been found to react readily with H_4SiO_4 forming silicate phases [19-22]. Given the important role of Sr in the phase decomposition of these cathode materials, the investigation of Sr-free materials for SOFC cathode applications seems highly appropriate.

The mixed ionic electronic conductor $\text{La}_2\text{NiO}_{4+\delta}$ (LNO) has been proposed as promising cathode material for SOFCs with a higher tolerance for Cr-poisoning [23]. LNO is the first member of the Ruddlesden-Popper series $\text{A}_{n+1}\text{B}_n\text{O}_{3n+1}$ ($n=1, 2, 3\dots$) with high oxygen diffusivity and sufficient electronic conductivity for SOFC cathode applications [24,25]. However, reports on the long-term stability of LNO against the combined effects of Cr- and Si-poisoning have been scarce. In a previous work, prolonged exposure of LNO to Cr and Si in dry and humid atmospheres at 700°C has

been shown to cause a significant decrease in surface activity due to a partial decomposition of the material [4,19].

This study intends to expand the existing knowledge on the influence of Cr- and Si-contaminants on LNO under SOFC operating conditions at 800°C. Test samples are exposed to Cr- and Si-sources in dry and humid O₂/Ar atmospheres and the degradation process is investigated via monitoring the chemical surface exchange coefficient of oxygen over time. Microstructural and chemical changes occurring on the sample surface are characterized using various analytical techniques and the crystal structures as well as the chemical composition of newly formed degradation phases are identified.

2 Experimental

2.1 Sample preparation

LNO powder (Treibacher Industrie AG) was isostatically pressed into a cylindrical pellet at 200 MPa and sintered two times for 10 h at 1350°C with heating and cooling rates of 2 K min⁻¹. The theoretical density of the sintered pellet was 98%. A rectangular sample with the dimensions 6×6×10 mm³ was cut with a diamond wire saw and the four larger faces were polished using polymer-embedded diamond lapping films with 30, 6 and 1 μm particle size. Electrical contacts (gold) were attached to both smaller faces using gold paste (Metalor) and two voltage probes were placed between the gold contacts at a distance of 5.2 mm from one another.

2.2 Electrical conductivity relaxation measurements

The influence of surface contamination via Cr- and Si-species on the oxygen exchange kinetics was determined at 800°C in dry and humid O₂/Ar atmospheres.

The electrical conductivity (σ) of the LNO sample was obtained from V/I characteristics in linear four-point geometry. Chemical surface exchange coefficients (k_{chem}) and chemical diffusion coefficients (D_{chem}) of oxygen were measured using the dc-conductivity relaxation method [26]. Oxidation and reduction steps were realized by changing the oxygen partial pressure around the sample ($0.1 \leq p\text{O}_2/\text{bar} \leq 0.15$). A constant current of 300 mA was applied and the electrical conductivity of the sample was recorded as a function of time. The gas flow was kept constant at $2 \text{ dm}^3 \text{ h}^{-1}$. SOFC operation with undried air was simulated by passing the gas streams through washing bottles filled with deionized water which were thermostatted at 6°C or 17°C , to achieve relative humidities (r.h.) of 30% and 60%, respectively (100% r.h. corresponds to the equilibrium vapor pressure of H_2O at 25°C). The kinetic parameters k_{chem} and D_{chem} were calculated from the conductivity response to sudden changes in oxygen content around the sample using non-linear regression analysis of the corresponding solutions of the two-dimensional diffusion equation [27]. The effects of simultaneous Cr- and Si-poisoning were simulated by placing the sample next to Cr-pellets in a quartz glass reactor, which served as a constant Si-source under humid conditions. Two additional samples of LNO positioned close to the measured sample were removed at different stages during the degradation study for chemical analysis. For a more in-depth description of the measurement procedure see Bucher [28].

2.3 X-ray photoelectron spectroscopy (XPS)

A Perkin Elmer PHI 5600 ESCA system with a hemispherical analyzer and a standard X-ray source (Mg-K α radiation, 1253.6 eV) was used to record XPS spectra of an area with 400 μm in diameter in constant analyzer mode. To check for impurities, survey scans were performed before depth profiling. For depth profiling an

Atomica WF 421 Microfocus Ion Gun was used to automatically scan a sample area of $1.2 \times 1.5 \text{ mm}^2$ with a 10 kV Ar^+ ion beam of approximately 150 μm diameter, irradiating the surface at an ion current of 125 nA. A sputter rate was estimated from the Ar^+ -fluence by assuming a yield of 2 target atoms per impinging Ar^+ , taking into account the volume density of the bulk composition [29]. The background was subtracted using a Shirley background function and the concentrations of the specific elements were obtained from the core-level peak areas by using standard relative sensitivity factors. The reproducibility of the XPS quantification amounts to about 1%.

2.4 Scanning electron microscopy with energy-dispersive X-ray spectroscopy (SEM-EDXS)

SEM images and EDXS analyses of sample surfaces were obtained using a Zeiss EVO50, equipped with a LaB_6 cathode and an Oxford Instrument INCA EDX detector at acceleration voltages of 15 kV. Elemental distribution maps of LNO were recorded at acceleration voltages of 10 kV using a Zeiss Ultra 55 microscope with an EDAX Phoenix EDXS detector.

2.5 High resolution scanning transmission electron microscopy (HR-STEM)

A Focused Ion Beam (FIB) NOVA 200 Nanolab dual beam microscope was used for TEM lamella preparation. Energy dispersive X-ray spectroscopy (EDXS) and electron energy loss spectroscopy (EELS) analyses were conducted using a FEI Tecnai F20 microscope operated at 200 kV in STEM mode. High resolution imaging was realized using a FEI Titan³ G2 60-300 microscope (operated at 300 kV) equipped with a C_s probe corrector (DCOR) for sub-Ångström resolution and a post-column energy filter (GIF Quantum ERSTM) from Gatan Inc. To determine the chemical composition of secondary phases, high resolution images were compared

with high angle annular dark field (HAADF) simulations calculated with the software package JEMS [30].

3 Results and discussion

3.1 Oxygen exchange kinetics

Conductivity relaxation measurements were performed over a period of approximately 4000 hours. A set of typical conductivity relaxation curves measured at different stages of the degradation study together with the corresponding fitting curves is given in Fig. 1. The sample geometry was optimized to allow for the simultaneous determination of the oxygen transport properties k_{chem} (Fig. 2a) and D_{chem} (Fig. 2b). Results obtained from the oxidation steps ($p\text{O}_2$ change from 0.1 to 0.15 bar) are indicated in blue while parameters obtained from the reduction steps ($p\text{O}_2$ change from 0.15 to 0.1 bar) are shown as red symbols. The electrical conductivity (Fig. 2c) was recorded between oxidation and reduction steps to check for changes in the bulk of the material during the degradation study. For the first 600 hours, the sample was kept in a dry O_2/Ar mixture at 800°C without a chromium source in order to determine the intrinsic stability of LNO. It should be mentioned that, since the measurements were conducted in a quartz glass reactor, a potential Si-source was always present at every step of the experiment. However, under dry conditions the volatilization of SiO_2 is practically negligible [14]. In dry atmospheres, k_{chem} and D_{chem} remained constant at values of $3.4 \times 10^{-3} \text{ cm s}^{-1}$ and $1.5 \times 10^{-4} \text{ cm}^2 \text{ s}^{-1}$ (average of oxidation and reduction steps), respectively, indicating excellent intrinsic stability of the material. Fig. 3 presents a comparison of average k_{chem} values obtained in this study with data reported by Li and Haugrud [31] and data from an earlier study by our group [32]. Arithmetic means and standard deviations were calculated based on 12 k_{chem} values measured in dry atmospheres at 800°C for

oxidation and reduction steps separately, as oxidation steps yield systematically higher k_{chem} values. The standard deviations amount to 7% for both oxidation and reduction reactions (k_{chem} (ox): $3.6 \times 10^{-3} \pm 2.4 \times 10^{-4} \text{ cm s}^{-1}$; k_{chem} (red): $3.2 \times 10^{-3} \pm 2.4 \times 10^{-4} \text{ cm s}^{-1}$). Although k_{chem} depends on several factors such as surface properties (quality of the polishing process, presence of impurities) and oxygen partial pressure, the values obtained in this study are in good agreement with published data. Cooling down to room temperature to repair a broken contact and reheating to 800°C did not have any impact on the measured parameters. After 600 hours, a Cr-source was added, and the relaxation measurements were continued under dry conditions for 1000 hours, resulting in a slight reduction of k_{chem} by a factor of 1.3. This is a clear indication of degradation processes affecting the sample surface. Since both D_{chem} and σ remained quite stable, there appears to be no impact on the bulk of the material. Similar observations were made in an earlier study, in which the slight decrease in oxygen exchange activity could be attributed to the formation of small chromium-containing crystallites on the sample surface [4]. However, once the test gas was humidified (30% r.h.) a sudden decrease of k_{chem} by a factor of 18 was recorded. As a result, D_{chem} could no longer be extracted from the measured conductivity profiles, indicating that the oxygen exchange reaction changed into a surface-controlled process. This can be attributed to the enhanced gas phase transport of volatile Cr-species ($\text{CrO}_2(\text{OH})_2$) as well as the formation of volatile Si-compounds (H_4SiO_4) in the presence of water vapor [3,14]. After 1000 hours under humid conditions in the presence of a Cr- and a Si-source the surface exchange coefficient stabilized at a value of $1.4 \times 10^{-4} \text{ cm s}^{-1}$. A further increase in humidity to 60% r.h. resulted in only a slight decrease in k_{chem} over the course of another 1000 hours. This is not very surprising considering that at 800°C the partial pressure of the most abundant Cr-vapor species ($\text{CrO}_2(\text{OH})_2$) only increases from

1.9×10^{-8} bar at 30% r.h. to 3.9×10^{-8} bar at 60% r.h. [6]. The electrical conductivity of the sample (Fig. 2c) remained quite constant during all stages of the experiment. In comparison to an earlier study by our group on the influence of Cr and Si on the oxygen exchange kinetics of LNO, where a decrease in k_{chem} by a factor of 230 was observed at 700°C [4], LNO seems to be much less prone to Cr/Si-degradation at 800°C, showing an overall drop in k_{chem} by only a factor of 25 under similar experimental conditions.

Since all measurements were performed in a quartz reactor acting as Si-source, the influence of humidity alone on the oxygen exchange properties of LNO could not be determined in this work. However, long-term tests on symmetrical cells with porous LNO electrodes under Si-free conditions at 800°C and 30% r.h. conducted by our group (data not yet published) showed that exposure to humidity in the absence of a Cr- and Si-source had no significant influence on the area specific resistance (ASR) of the electrodes over a period of 650 hours. However, once a Cr-source was introduced in addition to humidity, a strong increase in the ASR was observed. This is consistent with the findings presented in this work and suggests that humidity alone does not affect the oxygen surface exchange process of LNO in a significant way.

3.2 Scanning electron microscopy with energy dispersive X-ray spectroscopy

To determine the cause for the reduction in oxygen surface exchange rates, SEM images of degraded samples removed at different stages of the degradation study were recorded. Fig. 4 displays images taken in backscattered electron (BSE) mode of (a) a polished and thermally etched LNO sample, (b) a sample tested for 600 hours without and 1000 hours with a Cr-source present in dry conditions, (c) a sample exposed for another 1000 hours to Cr in moderately humidified atmospheres

(30% r.h.) and (d) a sample subjected for additional 1000 hours to a strongly humidified atmosphere (60% r.h.).

The polished and etched sample displayed in Fig. 4a features grains with diameters of 5 to 10 μm . Analysis of the sample surface using EDXS reveals a La:Ni cation ratio of 2:1, while impurity levels are well below the detection limit of the method. A second analysis of a polished sample of the same sintered compact, however, revealed the presence of small NiO inclusions along the grain boundaries of LNO grains (data not shown). The second sample (Fig. 4b) – exposed to Cr/Si-sources for a period of 1000 hours in dry atmospheres – shows large LNO grains covered with smaller crystallites as well as sporadic patches of dark contrast, identified as Zr- und Si-containing phases by EDXS. These secondary phases are believed to be formed from material impurities and not to be the result of contamination via gas phase transport, as traces of Si (90 ppm) were found in the raw material and Zr was likely introduced by powder milling. As already mentioned, Si and SiO_2 do not form volatile gas species in O_2/Ar in the absence of water vapor [14] and thus the quartz glass reactor cannot be the source of Si-compounds formed on the sample surface in dry atmospheres.

In addition, small amounts of Bi are detected in regions of fine crystalline structures, originating from the gold paste used for contacting the sample. However, neither the Bi-contaminants nor the corresponding morphological changes seem to have a significant influence on the oxygen exchange reaction. Figs. 4c and 4d depict sample surfaces exposed to O_2/Ar gas streams with 30% and 60% r.h., respectively. The surfaces are densely covered in fine crystallites. EDXS point analyses at several different regions of the degraded surfaces confirm the presence of Cr, Si and Bi.

To obtain a clearer picture about the distribution of elements on the degraded sample surface, detailed EDXS analyses of the sample subjected to 60% r.h. in the

presence of Cr and Si were conducted. Fig. 5 displays a secondary electron (SE) image of a selected surface region as well as the corresponding elemental distribution maps of La, Ni, O, Cr and Si. Finely dispersed dark spots in the La-map – indicating a local depletion of La and coinciding with high concentrations of Ni in the Ni-map – are caused by NiO impurities. On a larger scale, La as well as O appear to be evenly distributed across the surface. Dark areas in the Cr-map correspond to high concentrations of Si in the Si-map and vice versa, thus indicating the formation of at least one Cr-rich and one Si-rich secondary phase, both of which also contain La and O. Furthermore, Ni seems to be depleted in areas rich in Si, but not in areas where Cr is present. Also, Bi was found in areas rich in Cr and devoid of Si (data not shown). It must be mentioned that parts of the La-signal may have been attributed to the Cr-map due to a strong overlap of the Cr-K α peak (5.410 keV) with the La-L β peak (5.372 keV) in the acquired EDX spectra. In a similar way, part of the Cr-signal may have been integrated into the O-map due to an overlap of the Cr-L α peak (0.573 keV) and the O-K α peak (0.525 keV). Nevertheless, these results are in good agreement with TEM results of an earlier study on the phase decomposition of LNO under Cr- and Si-poisoning conditions at 700°C [19], which confirmed the formation of La-chromate and La-silicate phases but did not permit the determination of their exact composition or crystal structure.

3.3 *X-ray photoelectron spectroscopy*

To gain some depth resolution regarding the composition of the near-surface degradation layer, XPS elemental depth profiles of La, Ni, O, Cr and Si were recorded at different stages during the long-term study (Fig. 6). Sputtering of the samples was continued until constant concentrations for La, Ni and O were reached.

The XPS depth profile of a fresh, undegraded sample presented in Fig. 6a shows a uniform depth distribution of La, Ni and O. The steep profile slopes at the immediate surface are due to high levels of carbon detected on the sample surface, which might be remnants of materials used for sample preparation or molecules adsorbed during storage in ambient air [22]. Fig. 6b displays the sample treated for 1600 h in dry O₂/Ar with a Cr- and Si-source present. An increased La:Ni ratio within the first 15 nm from the surface, followed by a zone with higher Ni content, indicates La segregation towards the surface. This phenomenon has been reported in the literature by several authors [33-36]. Small amounts of Cr and Si are detected which may be responsible for the slight decline of k_{chem} in dry atmospheres (see section 3.1).

After additional 1000 hours in moderately humidified atmosphere (30% r.h.) a degradation layer of approximately 800 nm thickness is formed, followed by a fairly constant concentration of La, Ni and O (Fig. 6c). The degraded surface layer shows an increased La:Ni ratio compared to the bulk and large amounts of Cr are found with a maximum at depths of approximately 400 nm. Si-species were detected up to 400 nm from the sample surface, with a large accumulation within the first 50 nm. Elemental profiles of the sample treated for another 1000 hours in strongly humidified O₂/Ar atmosphere (60% r.h.) are presented in Fig. 6d. The degradation layer has grown by approximately 200 nm in this last phase of the degradation study, which surprisingly did not cause a further decline in oxygen surface exchange rates (see section 3.1). The near-surface layer is almost completely depleted of Ni while the Cr-profile indicates a pronounced accumulation of chromium within the first 200 nm, followed by a broad plateau. Si-species were found to be deposited at the immediate surface and interspersed with Cr-rich regions up to depths of 600 nm.

Fig. 7 shows the evolution of peaks selected for the quantification of Cr ($2p_{3/2}$) and Si ($2s$) together with Bi ($4f$) during XPS depth profiling. Hatched areas mark the range of measured binding energies for oxides of Cr, Si and Bi taken from the NIST X-ray Photoelectron Spectroscopy data base [37].

XPS spectra of the Cr $2p_{3/2}$ region recorded in the near-surface zone (Fig. 7, left) suggest the presence of Cr(III) oxide compounds, while no signals of Cr(VI) species (e.g. chromate CrO_4^{2-} or dichromate $\text{Cr}_2\text{O}_7^{2-}$) are detected. With increasing sputtering depths, a second peak emerges at lower binding energies which can be attributed to metallic Cr. The deposition of Cr in metallic form is highly implausible considering the high temperatures and oxidizing conditions applied in the degradation study and is most likely an artifact caused by prolonged Ar^+ ion bombardment in the course of the sputtering process during depth profiling. The reduction of metal oxides due to sputtering with Ar^+ ions has been described in the literature for Cr [38,39] and other transition metals [21,22,40-42]. Other elements with similar binding energies as metallic Cr would be Ag ($3p_{3/2}$) and Te ($3d_{5/2}$) which, however, are not contained in any of the materials used in the experimental setup and have not been detected by any of the other analytical methods applied in this work.

Signals at binding energies consistent with Si(IV) oxides have been identified (Fig. 7, right) which – together with results from SEM analysis – points to the formation of a lanthanum silicate phase. No evidence of metallic silicon can be found. Signals of bismuth are also clearly visible in the surface scan, but quickly disappear after the first few sputtering steps, indicating that Bi contaminations are only present at the topmost surface layer.

Based on the XPS results it is difficult to get a conclusive picture about the elemental distributions within the surface layer. Looking at Fig. 6c (after 1000 h at

30% r.h.) it appears that the topmost reaction layer is composed of a Si-compound beneath which a Cr-containing phase is located. This is plausible, considering the higher volatility of CrO₃ in dry atmospheres as compared to SiO₂, which should lead to preferential Cr-poisoning in the early stages of the degradation study (dry atmospheres) while Si is deposited at a later stage when humidity is added to the gas stream. This model, however, is somewhat contradicted by the XPS depth profiles recorded after exposition to 60% r.h. (Fig. 6d).

It should be mentioned that due to the large lateral averaging of the XPS technique (400×400 μm²) the interpretation of the depth profiles is not straightforward, as it would have to be based on the assumption of a rather evenly layered structure of the surface zone. This, however, seems not to be the case according to SEM results presented in the previous section, which show the degraded surface layer to be laterally inhomogeneous at a length scale smaller than the area analyzed by XPS (see Fig. 5).

In order to get a clearer picture about the make-up of the near-surface region and to allow for phase identification of the Cr- and Si-containing secondary phases, TEM analyses were conducted.

3.4 High resolution scanning transmission electron microscopy

A STEM HAADF cross section image of the decomposed surface layer is displayed in Fig. 8a. The HAADF Z-contrast reveals an approximately 1 μm thick near-surface degradation zone containing various phases of different chemical composition. In the topmost layer, marked as region 1 in Fig. 8a, La, Si and O are confirmed by EDXS. Complementary electron energy loss spectroscopy (EELS) measurements show that neither Cr nor Ni are present within this layer. The small grains marked as region 2 below the topmost layer are identified as La-Cr-Ni-oxide.

Due to the small crystallite size, the exact chemical composition could not be reliably determined by EDXS. Dark grains in region 3 are identified as NiO by EDXS and EELS. Similar inclusions are also clearly visible in the elemental distribution map of Ni presented in section 3.2. Since NiO was also found in a fresh sample, its presence cannot be unambiguously assumed to be caused by secondary phase formation during the degradation process. For comparison, an EDX spectrum of the bulk composition (region 4) is depicted in Fig. 8b.

Detailed structural information of the La-Si-O and La-Cr-Ni-O secondary phases were obtained in HR-STEM mode (Figs. 9 and 10). The Si-rich layer (analyzed area marked by a white circle in Fig. 9a) is identified as silicon oxyapatite $\text{La}_{9.33}(\text{SiO}_4)_6\text{O}_2$ with space group $P6_3/m$ (176) by comparison of an HAADF-simulation (white rectangle in Fig. 9b) of this compound with the acquired high resolution image. The comparison of a calculated Fast Fourier Transformation (FFT) based on the HR-STEM image with the simulated diffraction pattern of $\text{La}_{9.33}(\text{SiO}_4)_6\text{O}_2$ in $[2 -1 -1 3]$ zone axis further supports this result. Interestingly, this highly anisotropic material exhibits significant ionic conductivity ($10\text{-}20 \text{ mS cm}^{-1}$ at 800°C [43]) – similar to that of YSZ – and has been investigated as electrolyte material for intermediate-temperature solid oxide fuel cells [44,45].

A similar procedure was carried out for the Cr-containing phase depicted in Fig. 10a. A HRTEM image of the area marked with a black circle is shown in Fig. 10b. The calculated FFT image (Fig. 10c) was successfully matched to the simulated diffraction pattern of a $\text{La}(\text{Cr},\text{Ni})\text{O}_3$ perovskite with space group $Pnma$ (62) (Fig. 10d) as suggested by results from EDXS and EELS analysis. EDXS line-scans from the top of a $\text{La}(\text{Cr},\text{Ni})\text{O}_3$ crystal towards the bulk phase show a decreasing Cr-concentration and a corresponding increase in Ni-content (data not shown), which is easily established since $\text{LaCr}_{1-x}\text{Ni}_x\text{O}_3$ supports complete solid solution on the

perovskite B-site [46]. It is difficult to conclude from the available data whether the observed chromium phases are formed by Cr-diffusion into a LaNiO_3 degradation phase, Ni-diffusion into a LaCrO_3 secondary phase or by a more complicated reaction scheme. The Cr-rich end member of the $\text{LaCr}_{1-x}\text{Ni}_x\text{O}_3$ series is a *p*-type electronic conductor which is used for interconnector plates in high-temperature SOFCs [47]. Compared with LNO, however, the electrical conductivity of LaCrO_3 is rather low (0.96 S cm^{-1} at 800°C in air [48]). A tendency for the formation of LaCrO_3 has also been reported for Cr-poisoning of symmetrical LNO half cells by Lee et al. [23]. The formation of secondary phases with some levels of ionic or electronic conductivity may explain why – despite the strong decomposition of the sample surface – significant activity for the oxygen surface exchange reaction is still retained. Light grey stripes in the bulk phase directly below the degraded surface zone (see Fig. 11a) are identified in HR-STEM images as stacking anomalies in the LNO phase (Fig. 11b). Monolayers of the $n=3$ member of the $\text{La}_{n+1}\text{Ni}_n\text{O}_{3n+1}$ Ruddlesden-Popper series (Fig. 11c) are found to be embedded between regular ($n=1$) LNO layers. The formation of these monolayers can probably be attributed to the initially observed and continuously propagating segregation of La to the sample surface, which also has been reported in the literature [49].

4 Conclusions

The influence of Cr and Si on the long-term stability of $\text{La}_2\text{NiO}_{4+\delta}$ (LNO) was investigated at 800°C in dry and humidified O_2/Ar atmospheres. The degradation was monitored by measuring the chemical surface exchange (k_{chem}) and the chemical diffusion coefficient (D_{chem}) of oxygen using the dc-conductivity relaxation technique over a period of approximately 4000 hours. Moreover, ancillary pieces of LNO have

been mounted close to the sample and were removed at different stages of the degradation study for SEM-EDX analysis and XPS depth profiling.

While LNO exhibits good stability in the presence of Cr/Si-sources under dry conditions, a strong reduction of the oxygen exchange activity occurs when humidity is added to the gas stream, as evidenced by a decrease in k_{chem} by a factor 25 over the course of 4000 hours. HR-STEM imaging in combination with EDXS and EELS measurements was employed to identify the reaction phases formed on the sample surface after combined Cr/Si-poisoning. The main finding is a decomposition of the LNO surface layer into a predominantly oxide ion conducting phase $\text{La}_{9.33}(\text{SiO}_4)_6\text{O}_2$ and a predominantly electronic conducting compound $\text{LaCr}_{1-x}\text{Ni}_x\text{O}_3$, resulting in the observed decrease in oxygen surface exchange activity. Below the degraded surface zone, stacking faults consisting of higher order Ruddlesden-Popper phases are visible in HR-STEM images and are probably caused by La-segregation to the surface. It has been shown in this work that LNO is strongly affected by contaminants transported via the gas phase when treated with humidified test gases. Since this has also been reported for other SOFC cathode materials [6,27,50,51], it can be concluded that operation of such systems with pre-dried air or oxygen would significantly improve the long-term stability of cathodes.

Acknowledgements

The financial support provided by the Austrian 'Klima- und Energiefonds' and AVL List GmbH (Austria) within the program 'Neue Energien 2020' (project no. 834431, project title ELTSECCS) is gratefully acknowledged. The authors thank Gerhard Hawranek (Montanuniversitaet Leoben) and Sanja Šimić (Centre for Electron Microscopy, Graz) for SEM-EDXS measurements, as well as Martina

Dienstleder (Centre for Electron Microscopy, Graz) for TEM lamella preparation.

Treibacher Industrie AG is acknowledged for providing $\text{La}_2\text{NiO}_{4+\delta}$ powder.

References

- [1] N. Shaigan, W. Qu, D.G. Ivey, W. Chen, *J. Power Sources* 195 (2010) 1529-1542.
- [2] S. Frangini, A. Masci, S.J. McPhail, T. Soccio, F. Zaza, *Mater. Chem. Phys.* 144 (2014) 491-497.
- [3] B.B. Ebbinghaus, *Combust. Flame* 93 (1993) 119-137.
- [4] N. Schrödl, E. Bucher, A. Egger, P. Kreiml, C. Teichert, T. Höschen, W. Sitte, *Solid State Ionics* 276 (2015) 62-71.
- [5] S.-N. Lee, A. Atkinson, J.A. Kilner, *J. Electrochem. Soc.* 160 (2013) F629-F635.
- [6] E. Bucher, C. Gspan, T. Höschen, F. Hofer, W. Sitte, *Solid State Ionics* 299 (2017) 26-31.
- [7] A. Kruk, A. Adamczyk, A. Gil, S. Kaç, J. Dąbek, M. Ziąbka, T. Brylewski, *Thin Solid Films* 590 (2015) 184-192.
- [8] S.N. Hosseini, F. Karimzadeh, M.H. Enayati, N.M. Sammes, *Solid State Ionics* 289 (2016) 95-105.
- [9] E. Konyshева, H. Penkalla, E. Wessel, J. Mertens, U. Seeling, L. Singheiser, K. Hilpert, *J. Electrochem. Soc.* 153 (2006) A765-A773.
- [10] R. Trebbels, T. Markus, L. Singheiser, *J. Fuel Cell Sci. Technol.* 7 (2009) 011013/1-6.
- [11] E. Bucher, C. Gspan, F. Hofer, W. Sitte, *Solid State Ionics* 230 (2013) 7-11.
- [12] A.J. Schuler, Z. Wuillemin, A. Hessler-Wyser, J. Van herle, *Electrochem. Solid-State Lett.* 14 (2011) B20-B22.
- [13] T. Horita, H. Kishimoto, K. Yamaji, M.E. Brito, Y. Xiong, H. Yokokawa, Y. Hori, I. Miyachi, *J. Power Sources* 193 (2009) 194-198.
- [14] N.S. Jacobson, E.J. Opila, D.L. Myers, E.H. Copland, *J. Chem. Thermodyn.* 37 (2005) 1130-1137.
- [15] E.J. Opila, N.S. Jacobson, D.L. Myers, E.H. Copland, *JOM* 58 (2006) 22-28.
- [16] S.P. Jiang, Y.D. Zhen, *Solid State Ionics* 179 (2008) 1459-1464.
- [17] D. Oh, E. Armstrong, D. Jung, C. Kan, E. Wachsman, *Proc. 11th Intern. Symp. Solid Oxide Fuel Cells (SOFC-XI)* edited by S.C. Singhal, Vienna, Austria (2009) p. 2871-2879.
- [18] C.C. Wang, T. Becker, K. Chen, L. Zhao, B. Wei, S.P. Jiang, *Electrochim. Acta* 139 (2014) 173-179.
- [19] N. Schrödl, E. Bucher, C. Gspan, A. Egger, C. Ganser, C. Teichert, F. Hofer, W. Sitte, *Solid State Ionics* 288 (2016) 14-21.
- [20] I. Kaus, K. Wiik, M. Dahle, M. Brustad, S. Aasland, *J. Eur. Ceram. Soc.* 27 (2007) 4509-4514.
- [21] E. Bucher, W. Sitte, F. Klauser, E. Bertel, *Solid State Ionics* 191 (2011) 61-67.
- [22] E. Bucher, W. Sitte, F. Klauser, E. Bertel, *Solid State Ionics* 208 (2012) 43-51.
- [23] S.-N. Lee, A. Atkinson, J. Kilner, *ECS Trans.* 57 (2013) 605-613.
- [24] E. Boehm, J.M. Bassat, P. Dordor, F. Mauvy, J.C. Grenier, P. Stevens, *Solid State Ionics* 176 (2005) 2717-2725.
- [25] F. Mauvy, C. Lalanne, J.M. Bassat, J.C. Grenier, H. Zhao, P. Dordor, P. Stevens, *J. Eur. Ceram. Soc.* 25 (2005) 2669-2672.
- [26] A. Egger, W. Sitte, *Solid State Ionics* 258 (2014) 30-37.
- [27] A. Egger, W. Sitte, F. Klauser, E. Bertel, *J. Electrochem. Soc.* 157 (2010) B1537-B1541.
- [28] E. Bucher, *BHM* 156 (2011) 423-428.

- [29] R. Behrisch, W. Eckstein, *Sputtering by Particle Bombardment, Topics in Applied Physics, Vol. 110*, Springer, Berlin Heidelberg, 2007.
- [30] P.A. Stadelmann, *Ultramicroscopy* 21 (1987) 131-145.
- [31] Z. Li, R. Haugrud, *Solid State Ionics* 206 (2012) 67-71.
- [32] A. Egger, *Rare earth nickelates as cathodes for solid oxide fuel cells*, PhD thesis, University of Leoben, Austria, Department of General, Analytical and Physical Chemistry, 2013.
- [33] J. Druce, H. Téllez, M. Burriel, M.D. Sharp, L.J. Fawcett, S.N. Cook, D.S. McPhail, T. Ishihara, H.H. Brongersma, J.A. Kilner, *Energy Environ. Sci.* 7 (2014) 3593–3599.
- [34] T. Akbay, A. Staykov, J. Druce, H. Tellez, T. Ishihara, J.A. Kilner, *J. Mater. Chem. A* 4 (2016) 13113-13124.
- [35] G. Amow, P.S. Whitfield, I.J. Davidson, R.P. Hammond, C.N. Munnings, S.J. Skinner, *Ceramics International* 30 (2004) 1635-1639.
- [36] J. Choisnet, N. Abadzhieva, P. Stefanov, D. Klissurski, J.M. Bassat, V. Rives, L. Minchev, *J. Chem. Soc. - Faraday Trans. 90* (1994) 1987-1991.
- [37] NIST X-ray Photoelectron Spectroscopy Database, NIST Standard Reference Database Number 20, Gaithersburg MD, 20899 (2000), 10.18434/T4T88K, Feb. 2018.
- [38] J.F. Weaver, H.A.E. Hagelin-Weaver, G.B. Hoflund, G.N. Salaita, *Applied Surface Science* 252 (2006) 7895-7903.
- [39] S. Suzuki, M. Oku, Y. Waseda, *Surf. Interface Anal.* 25 (1997) 161-166.
- [40] T.J. Chuang, C.R. Brundle, K. Wandelt, *Thin Solid Films* 53 (1978) 19-27.
- [41] S. Suzuki, K. Sugiyama, Y. Waseda, *Journal of Surface Analysis* 9 (2002) 455-458.
- [42] S. Hashimoto, C. Tanaka, A. Murata, T. Sakurada, *Journal of Surface Analysis* 13 (2006) 14-18.
- [43] S. Nakayama, M. Sakamoto, *J. Eur. Ceram. Soc.* 18 (1998) 1413-1418.
- [44] X.G. Cao, S.P. Jiang, *Int. J. Hydrogen Energy* 41 (2016) 1203-1212.
- [45] D. Marrero-López, M.C. Martín-Sedeño, J. Peña-Martínez, J.C. Ruiz-Morales, P. Núñez, M.A.G. Aranda, J.R. Ramos-Barrado, *J. Power Sources* 195 (2010) 2496-2506.
- [46] J. Yang, *Acta Crystallogr. B* 64 (2008) 281-286.
- [47] T.S. Zhao, N. Meng (Eds.), *Solid oxide fuel cells: From materials to system modeling*, RSC Publishing, Cambridge, UK, 2013.
- [48] S.P. Jiang, L. Liu, K.P. Ong, P. Wu, J. Li, J. Pu, *J. Power Sources* 176 (2008) 82-89.
- [49] N. Gauquelin, T.E. Weirich, M. Ceretti, W. Paulus, M. Schroeder, *Monatsh. Chem.* 140 (2009) 1095-1102.
- [50] L. Zhao, J. Zhang, T. Becker, S.P. Jiang, *J. Electrochem. Soc.* 161 (2014) F687-F693.
- [51] X. Chen, Y. Zhen, J. Li, S.P. Jiang, *Int. J. Hydrogen Energy* 35 (2010) 2477-2485.

Figure captions

Fig.1. Conductivity relaxation curves of the oxidation process after (1) 552 h, (2) 1872 h and (3) after 3960 h. Measured data points are shown as black symbols while fitting curves applied for the calculation of k_{chem} values are plotted as grey dashed lines.

Fig. 2. (a) Chemical surface exchange coefficients of oxygen, (b) chemical diffusion coefficient of oxygen and (c) electrical conductivity of LNO at 800°C and $p\text{O}_2 = 0.1$ bar as a function of time. Chromium was introduced after approximately 600 hours. Experiments were conducted in a quartz glass reactor which served as a Si-source.

Fig. 3. Comparison of published chemical surface exchange coefficients of oxygen for LNO. Open gray symbols represent data from Li and Haugrud [31], black stars are data taken from Egger [32]. The blue and red filled symbols illustrate average values of k_{chem} for the oxidation (blue square) and the reduction (red diamond) reaction, calculated from k_{chem} values measured at 800°C in dry O_2/Ar mixtures over a period of 22 days.

Fig. 4. SEM images in BSE imaging mode of (a) a polished and thermally etched LNO sample, (b) after 600 h in dry atmosphere without Cr (but with Si) and 1000 h in a dry O_2/Ar mixture with Cr and Si at 800°C, (c) after an additional 1000 h in a humidified O_2/Ar gas mixture with 30% r.h. and (d) after another 1000 h in a humidified O_2/Ar gas mixture with 60% r.h.

Fig. 5. Post-test SEM image (top left) and corresponding SEM-EDXS elemental distribution maps of LNO after degradation at 800°C in 60% r.h. The width of all images is 108.54 μm .

Fig. 6. XPS elemental depth profiles of La, Ni and O in LNO and Cr/Si-impurities of (a) the freshly polished sample, (b) after 600 h in dry atmosphere without Cr (but with Si) and 1000 h in a dry O₂/Ar mixture with Cr and Si at 800°C, (c) after an additional 1000 h in a humidified O₂/Ar gas mixture with 30% r.h. and (d) after another 1000 hours in a humidified O₂/Ar gas mixture with 60% r.h.

Fig. 7. XPS spectra of the LNO sample after completion of the degradation study showing the evolution of signals of Cr 2p_{3/2}, Si 2s and Bi 4f during surface depth profiling.

Fig. 8. Post-test STEM HAADF image of (a) the near-surface region of LNO after degradation at 800°C in 60% r.h. and (b) corresponding EDX spectra of secondary phases. Additional peaks of Fe and Co originate from the interior lining of the microscope.

Fig. 9. (a) STEM HAADF image of the near-surface region of LNO with a white circle marking an area within the Si-rich secondary phase, (b) HR-STEM HAADF image of the marked area with HAADF simulation overlay (white rectangle), (c) FFT image of the selected area and (d) simulated diffraction pattern of La_{9.33}(SiO₄)₆O₂ in [2 -1 -1 3] zone axis. The red arrows a and b indicate the diffraction planes (-1 0 1) and (0 1 0), respectively.

Fig. 10. (a) STEM HAADF image of the near-surface region of LNO with a black circle marking an area within the Cr-rich secondary phase, (b) HR-STEM HAADF image of the marked area, (c) FFT image of the selected area and (d) simulated diffraction pattern of a perovskite structure with space group *Pnma*. Red arrows a and b indicate the diffraction planes (1 0 -1) and (0 -1 0), respectively.

Fig. 11. (a) STEM HAADF image of the bulk area below a degraded surface region of LNO after degradation at 800°C in 60% r.h., (b) HR-STEM HAADF image of the selected area with red lines indicating boundaries between the $\text{La}_2\text{NiO}_{4+\delta}$ main phase ($n=1$) and $\text{La}_4\text{Ni}_3\text{O}_{10}$ -type stacking faults and (c) crystal structure of the first three Ruddlesden-Popper phases $\text{A}_{n+1}\text{B}_n\text{O}_{3n+1}$ ($n=1, 2, 3$).

Figures

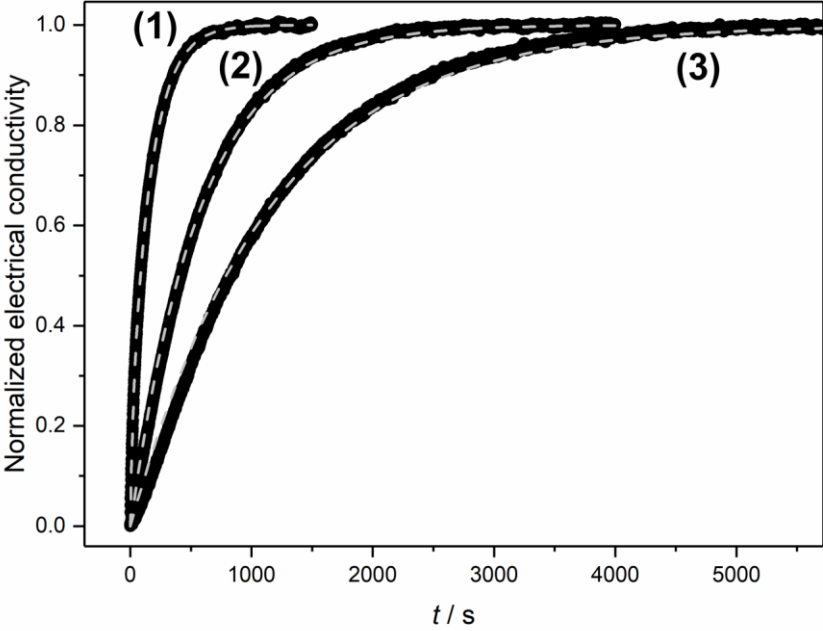


Figure 1.

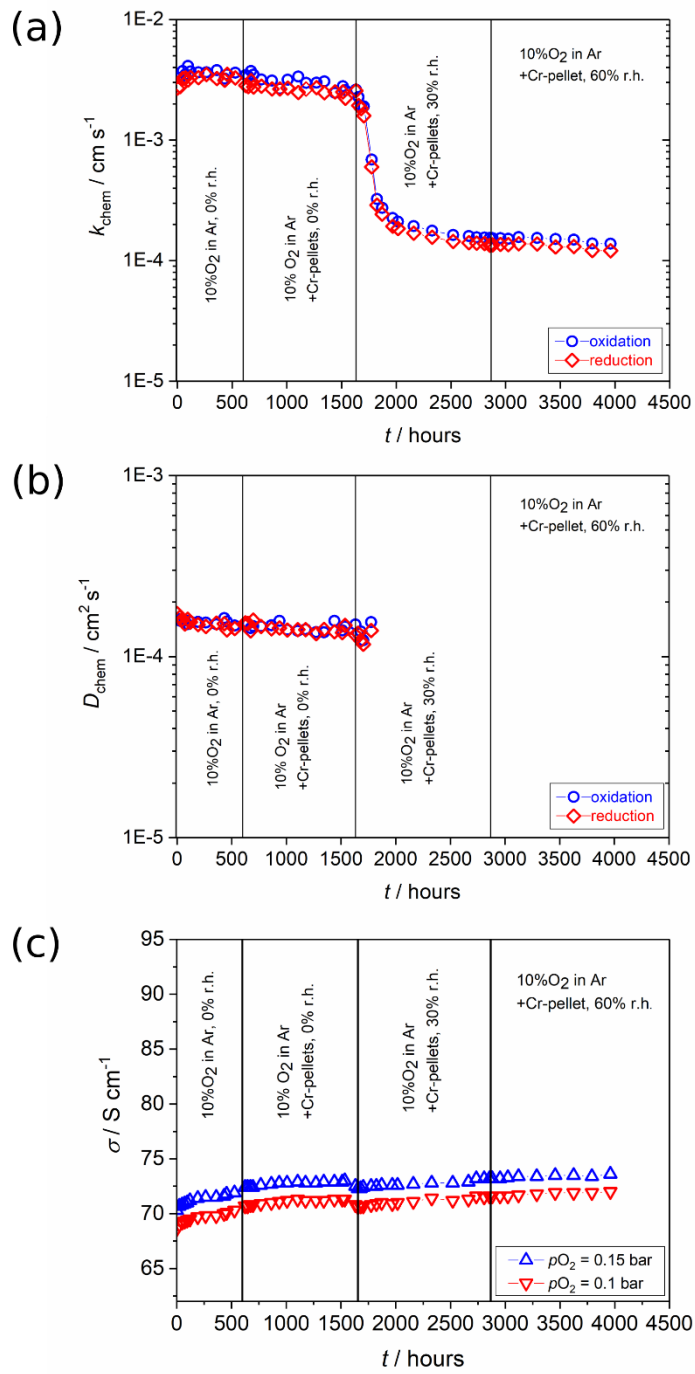


Figure 2.

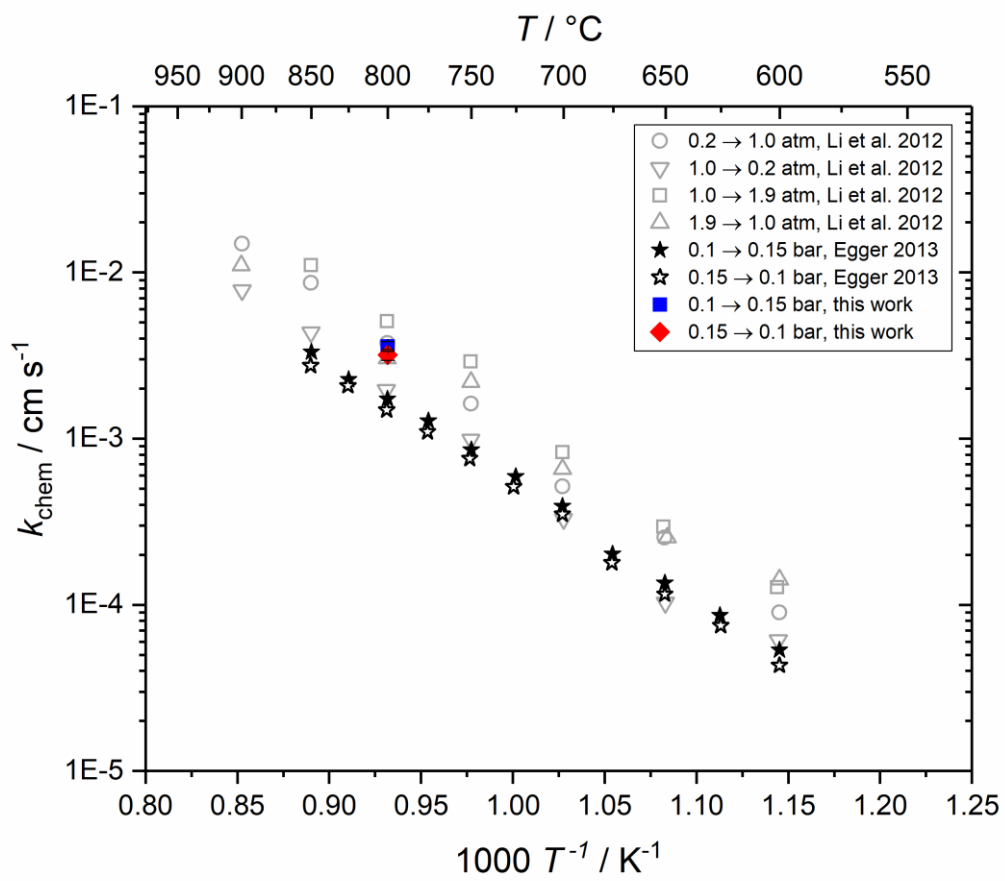


Figure 3.

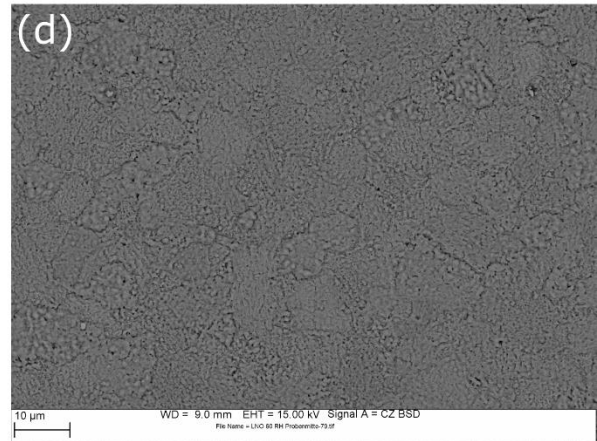
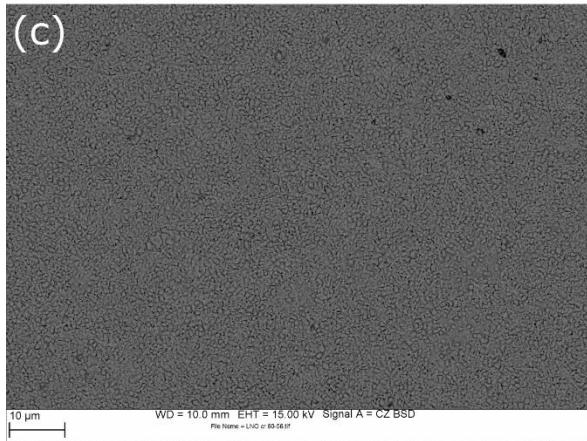
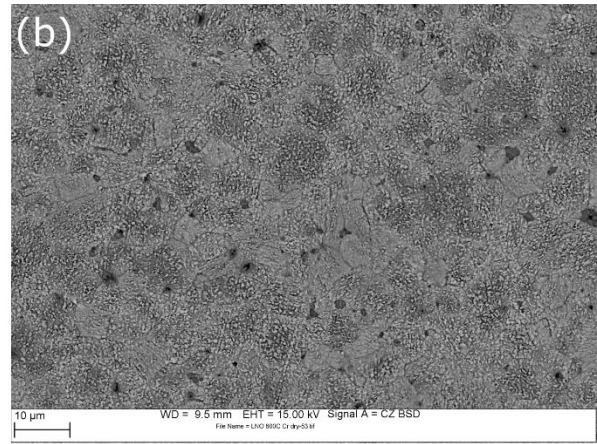
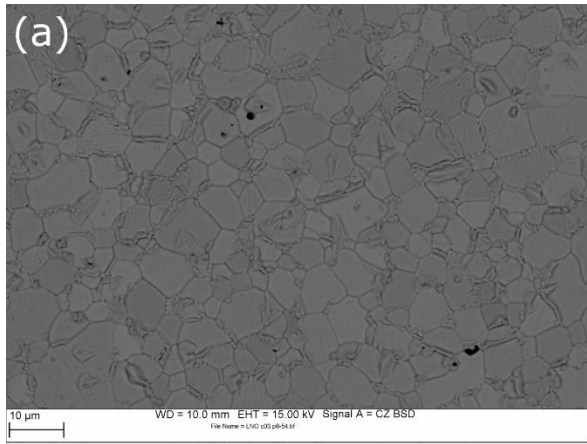


Figure 4.

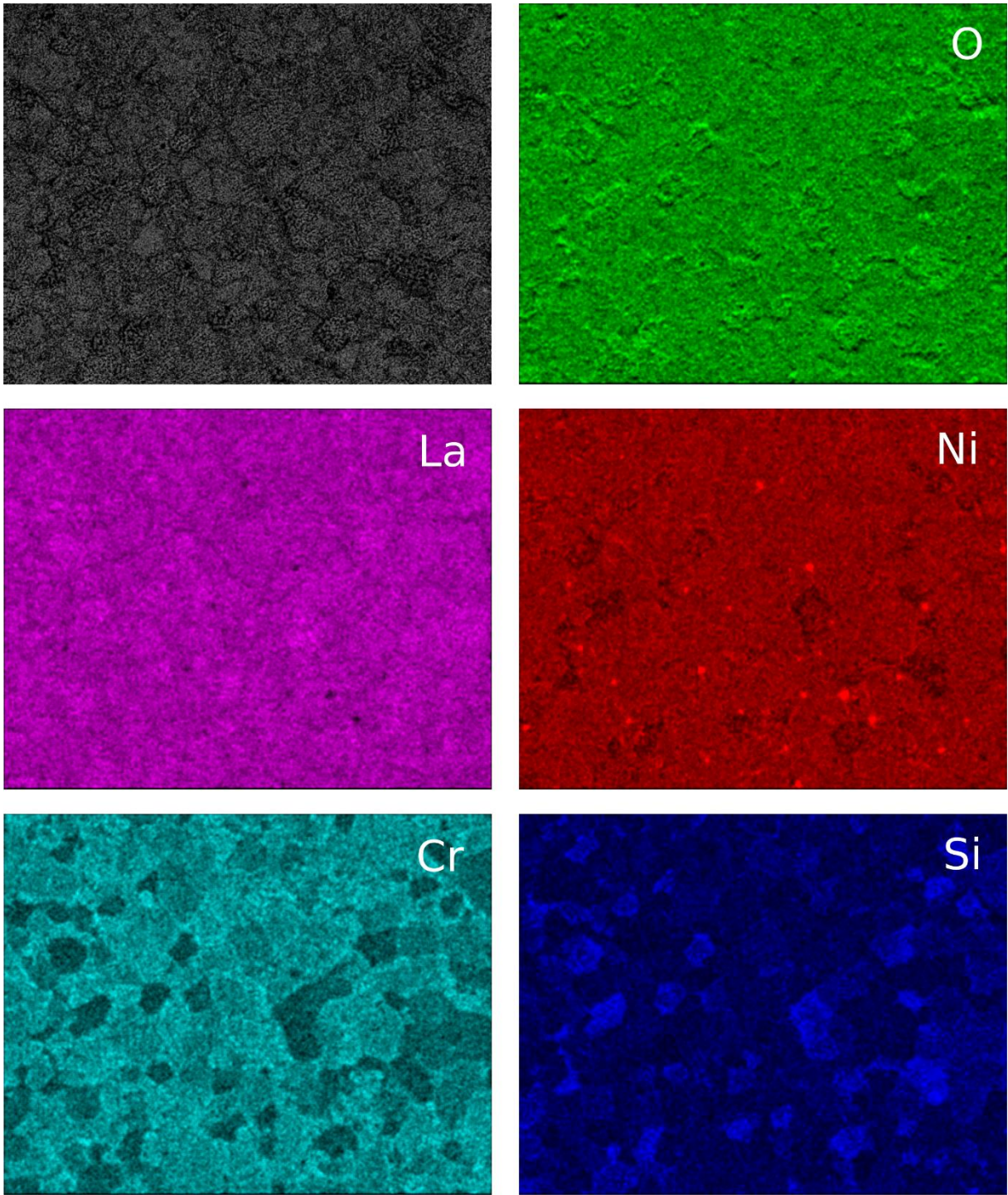


Figure 5.

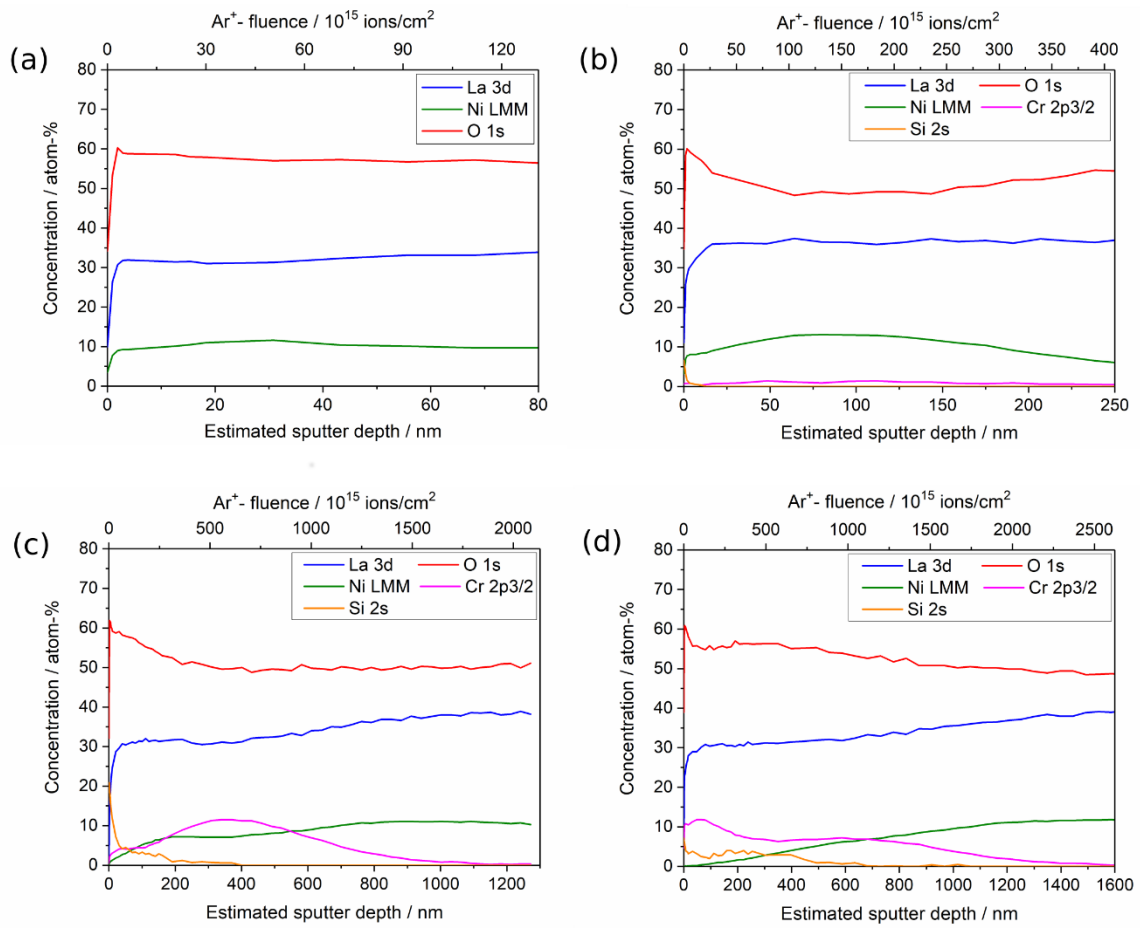


Figure 6.

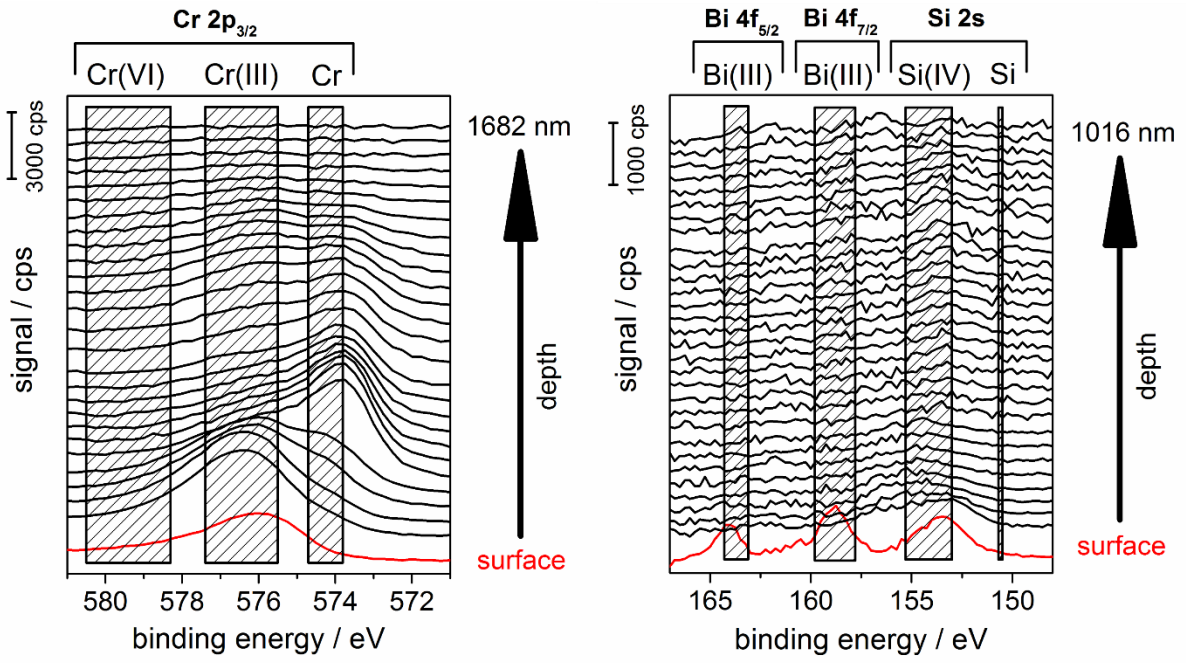


Figure 7.

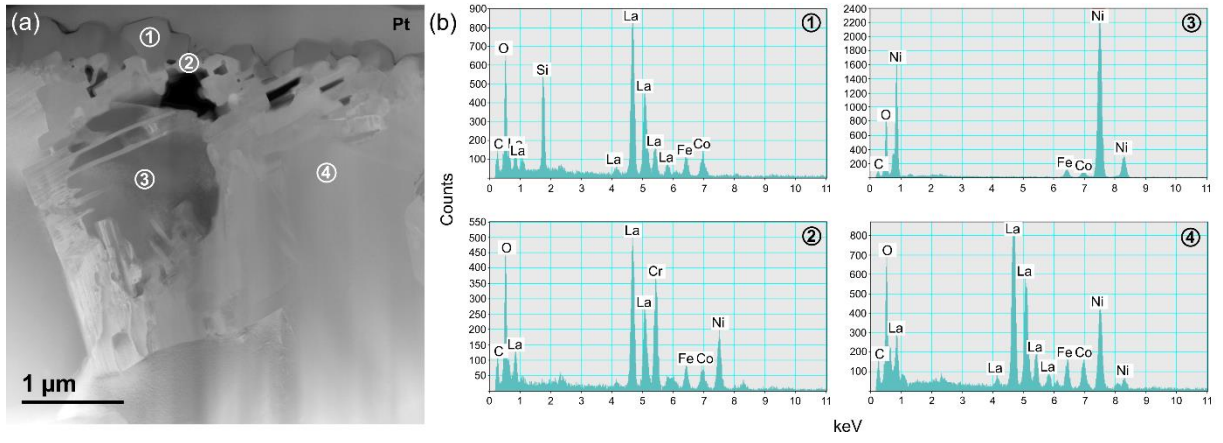


Figure 8.

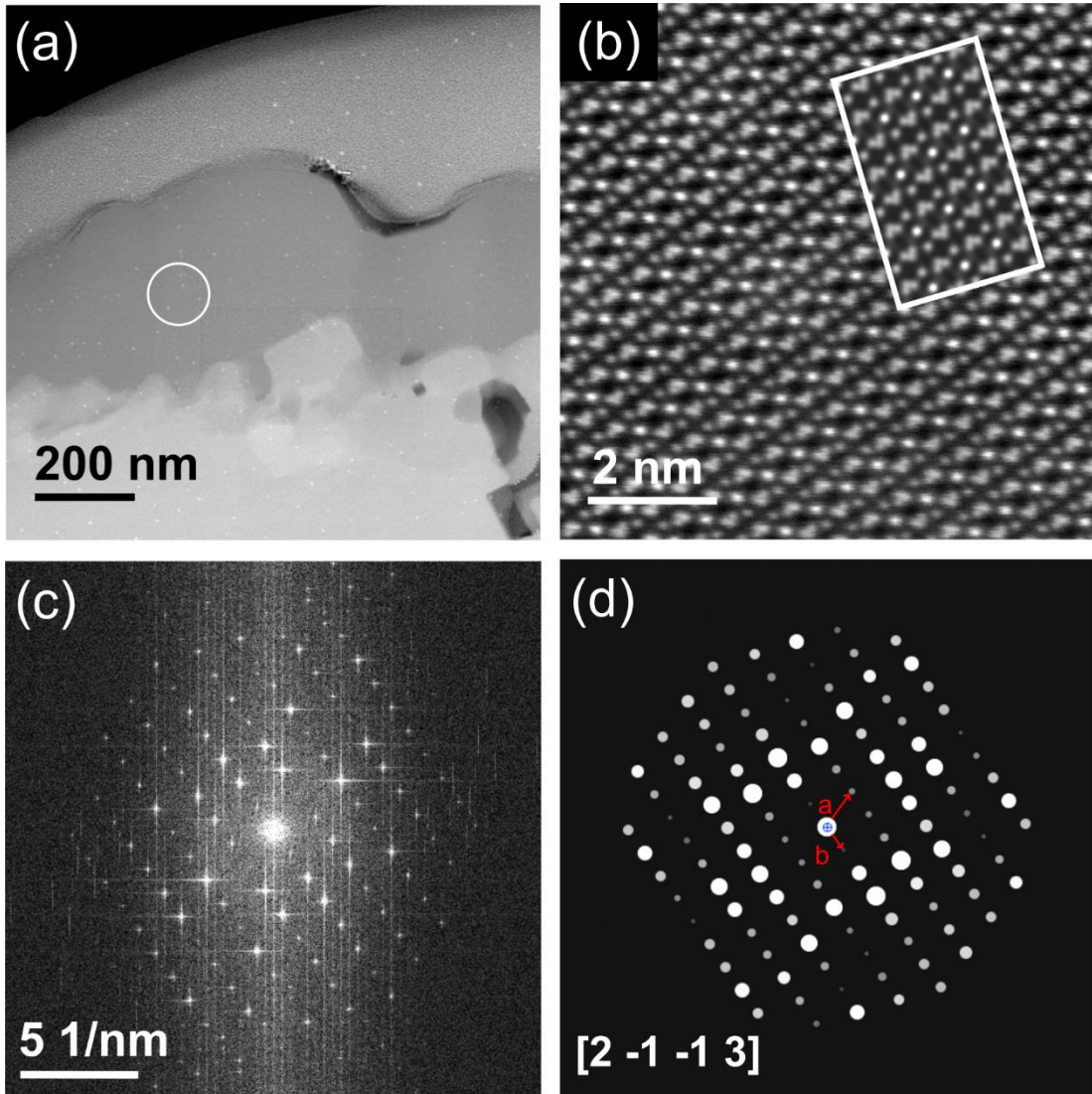


Figure 9.

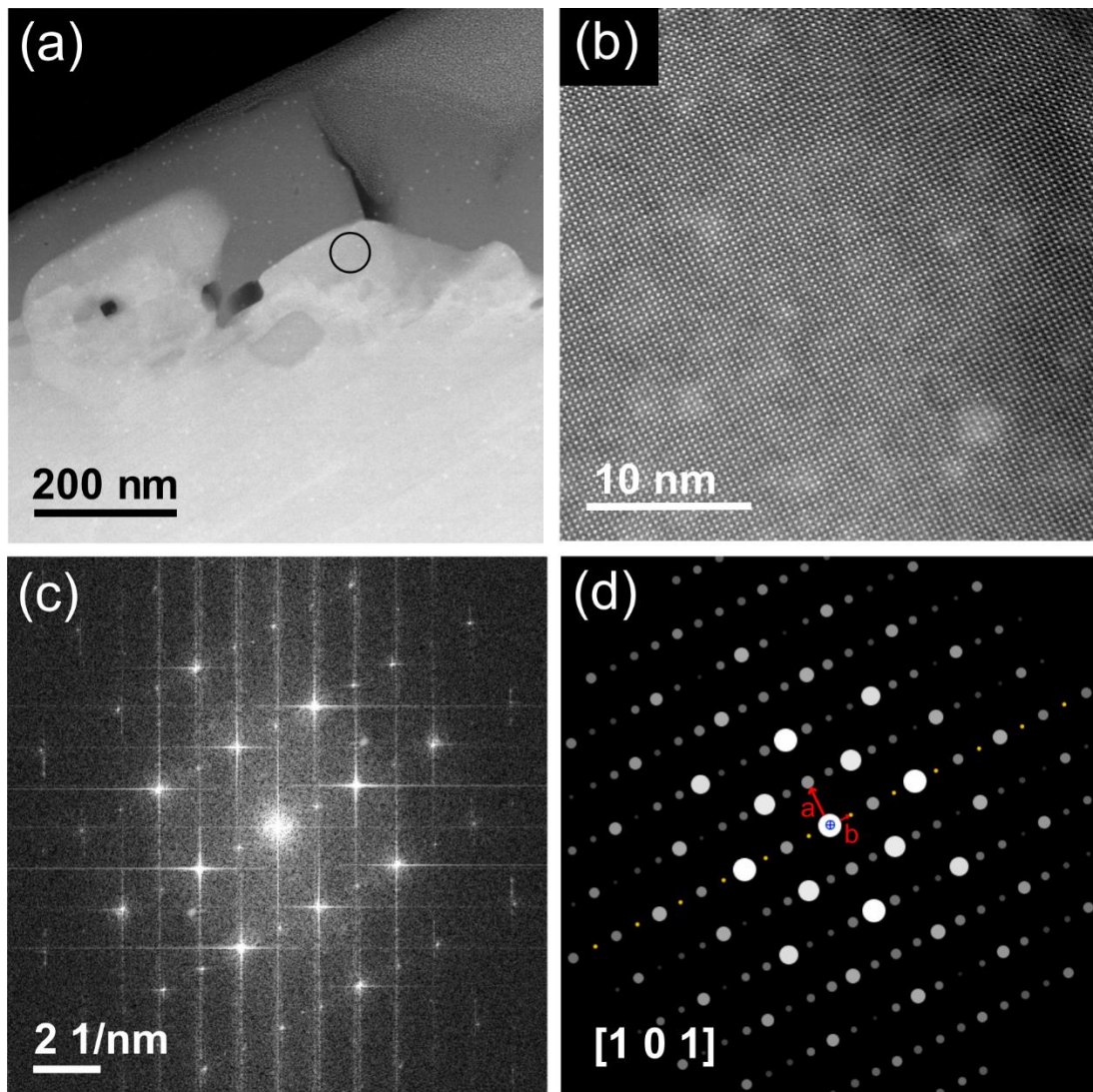


Figure 10.

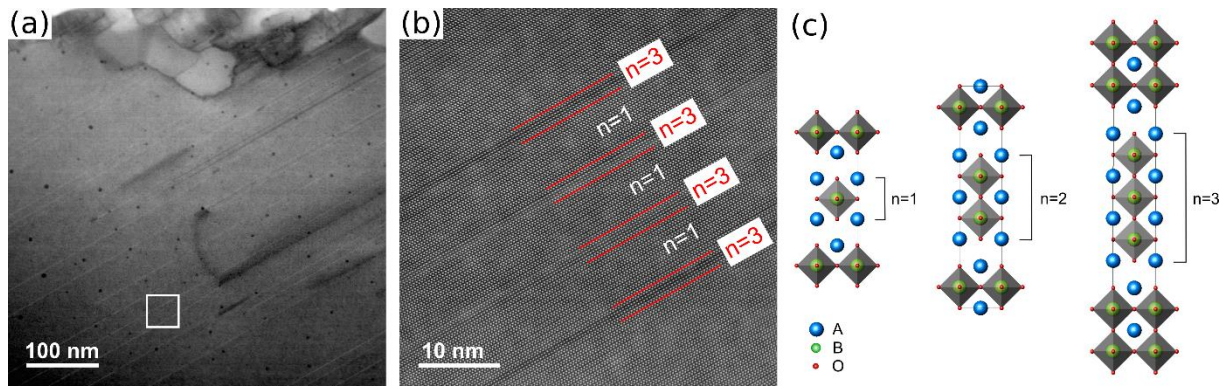


Figure 11.